Soft Materials with Broadband and Near-Total Absorption of Sound

Shichao Cui and Ryan L. Harne*

Department of Mechanical and Aerospace Engineering, The Ohio State University, Columbus, Ohio 43210, USA

(Received 8 October 2019; published 27 December 2019)

Low- and broadband-frequency sound absorption promotes myriad practical applications and scientific endeavors. Yet emerging metamaterial concepts enable such sound absorption only by the use of a complex assembly of attenuator constituents or by the addition of heavy undesirable mass. In this study, multiple low-frequency hybrid resonances are achieved in a soft-lightweight-material-based Helmholtz resonator. By replacing the rigid walls of a traditional Helmholtz resonator with compliant walls and by tailoring the relative structural and acoustic compliances, a unique multiphysics coupling among the material, structure, and sound is realized. These coupling mechanisms yield hybrid resonances that can be used for subwavelength, broadband, and near-total absorption of sound. As a result, the compliant-material resonator exploits a lightweight-material monolithic design that exerts dramatic and tunable control over low-frequency and broadband acoustic-energy transfer. This paper details analytical and experimental investigations to test the concept and reveals strategies for near-total absorption at arbitrary subwavelength frequencies.

DOI: 10.1103/PhysRevApplied.12.064059

I. INTRODUCTION

Low-frequency sound attenuation is of long-standing interest to science and society, whether to realize nonreciprocal wave propagation, to insulate interior spaces from exterior noise, or for a wide range of other purposes. Porous or barrier materials are commonly used to control low-frequency acoustic waves. Yet, these materials must be used in large heavy quantities to suppress the long wavelengths of low-frequency sound, and tuning strategies for these materials usually involve major changes to material-system dimensions and mass. Investigations of subwavelength sound-absorbing materials aimed at introducing unique potentials for tuning and to reduce the challenges imposed by added mass are abundant [1–6]. Acoustic metamaterials and metasurfaces, which exhibit properties not found in natural materials [7–9], enable programmable attenuation of low-frequency sound via subwavelength constituents whose collective behavior allows unusual macroscopic wave propagation [10–24].

Soft compliant materials and structural members are widely utilized as constituents in metamaterials to introduce coupling mechanisms that manipulate acoustic waves [1,14,25–28]. Soft-material-based membrane-type metamaterials may match the impedance between the acoustic fluid and the metamaterial to provide near-perfect absorption of sound [1,14,28]. Yet, these concepts are inherently effective for attenuating only single-frequency waves, so that broadband frequency attenuation requires a complex parallel assembly of constituents [14]. In fact, modifications to traditional Helmholtz resonators (HRs) [29–32] composed of more rigid materials may lead to a negative dynamic modulus [33], low-frequency wave absorption [34], and means of achieving multifrequency attenuation using embedded soft structural members [35,36]. Yet, unless heavy masses are added to reduce the frequency of resonance phenomena, the control of sound with such HR-based metamaterials remains limited to the mid frequencies, such as those greater than 300 Hz. To enable near-total absorption of the more intrusive low- and broadband-frequency sound, an approach is needed that does not rely on complex metamaterial assembly or a heavy mass that lessens versatility and robustness.

Among the many strategies by which one can tailor and enhance sound absorption in metamaterials, scientists may leverage principles from materials science and mechanics via integration of soft structural members to enable novel interactions between material behavior and acoustic-wave propagation [14,37]. Yet, there is a lack of knowledge on how to achieve extreme absorption of sound over a broad low-frequency range (e.g., less than 300 Hz) using such a combination of principles without resorting to a complex metamaterial assembly or to heavy mass. In this paper, we investigate a compliant-material resonator (CMR), a soft-material-based Helmholtz resonator, that enables unique subwavelength, broadband, and near-total absorption of sound with a monolithic material design. By replacing the rigid walls of a traditional HR with strategically designed compliant walls, multiple hybrid resonances are created at frequencies less than 300 Hz for exceptional broadband

*harne.3@osu.edu

control of sound. The paper describes the theory needed to characterize these intricate influences, and the results of efforts to experimentally confirm the efficacy of the concept of the CMR.

II. MODEL FOR SOUND ABSORPTION BY A COMPLIANT-MATERIAL RESONATOR

The CMR is a soft-walled cavity with a compact opening. The particular shapes of the walls and opening and the bulk compliant material may be selected in a vast number of combinations. In this paper, we study a model CMR that has six square walls that enclose a cubic inner cavity. Here, the side lengths of the inner cavity are much smaller than the acoustic wavelengths considered. A circular opening is made through one of the square walls to interface with the cavity and with the external acoustic pressure that is absorbed. The geometry of the CMR is shown in Fig. 1. A cross section of the CMR is also presented in Fig. 1 to illustrate the internal geometry and the coupling among the wall deflection, the inner acoustic pressure, and the motion of the air mass in the opening. See Appendix B for details.

In this work, the CMR is molded from silicone rubber with a constant wall thickness, and 3D printed annular necks are securely placed in the opening in the wall to tune the diameter and length of the cylindrical opening. The displacement w of the compliant wall and the inner pressure field p are coupled at the inner surfaces of the wall. Then, the displacement of the lumped air mass in the opening ξ is driven by a combination of the inner acoustic pressure p and an external plane wave excitation $Pe^{j\omega t}$, using complex time-harmonic notation. In this way, the resonances of the CMR are more intricately determined than for traditional HRs. This is because the compliant walls of the CMR permit low-frequency structural vibrations that engage with the acoustic field to yield multiple hybrid low-frequency resonances and thus near-total sound absorption across a broad frequency range.

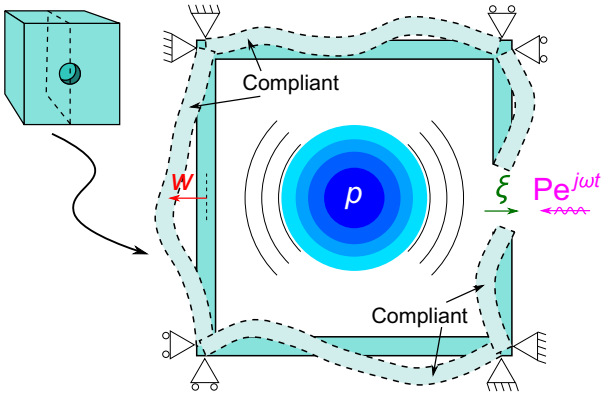

FIG. 1. Schematic illustration of the complete compliant-material resonator and a cross-section. The wall displacement is denoted by w, the inner acoustic-pressure field is represented by p, the displacement of the lumped air mass in the opening is expressed using ξ, and the harmonic plane wave excitation is denoted by $Pe^{j\omega t}$.

A model of the CMR is generalized to investigate the multiphysics couplings and mechanisms in the system. The set of governing equations is given in Eqs. (1)–(3), where q_m is the mth modal displacement of the wall:

$$\ddot{P}_n + \omega_{An}^2 P_n + \frac{A_A}{V}\rho_0 c_0^2 \sum_r \frac{\dot{P}_r C_{nr}}{M_r^A} = -\sum_m \frac{A_F}{V} L_{nm}\ddot{q}_m - \frac{1}{V}\ddot{\xi}\int_{A_{\mathrm{HR}}} F_n\, dA, \tag{1}$$

$$D_w(\ddot{q}_m + \omega_m^2 q_m) = \rho_0 c_0^2 A_F \sum_n \frac{P_n L_{nm}}{M_n^A}, \tag{2}$$

$$m\ddot{\xi} + R\dot{\xi} = A_{\mathrm{HR}}\rho_0 c_0^2 \sum_n \frac{P_n F_n}{M_n^A} + A_{\mathrm{HR}} P e^{j\omega t}. \tag{3}$$

Details of the derivation of the model, the expressions for the coefficients, and solutions for the structural-acoustic responses are presented in Appendix A. The specific acoustic impedance Z of the CMR is obtained by solving the governing equations of the system. Using the model solutions to determine the absorption coefficient α for the CMR leads to the result

$$\alpha = 1 - \left|\frac{Z/Z_0 - 1}{Z/Z_0 + 1}\right|^2, \tag{4}$$

where Z_0 is the specific acoustic impedance of air.

III. ORIGINS OF HYBRID BROADBAND RESONANCES AT LOW FREQUENCIES

The mechanisms governing the emergence of multiple low-frequency hybrid resonances in the CMR are uncovered by an analytical study of model results compared with results for a traditional rigid HR. The frequency dependence of the absorption coefficient for a range of opening radii is presented in Fig. 2, contrasting a traditional rigid HR and a CMR designed with the same geometric parameters. The dark red shading in Fig. 2 indicates near-total sound absorption. The rigid HR and the CMR both have an internal side length of the cubic cavity of 11 cm and a neck length of 1.7 cm. The CMR has a wall thickness of 10 mm. The material properties of the walls of the CMR are Young's modulus 500 kPa, Poisson's ratio 0.49, and density 1145 kg/m^3. For the rigid HR, the walls are assumed to be rigid such that the material properties and the thickness of the walls do not influence the absorption coefficient.

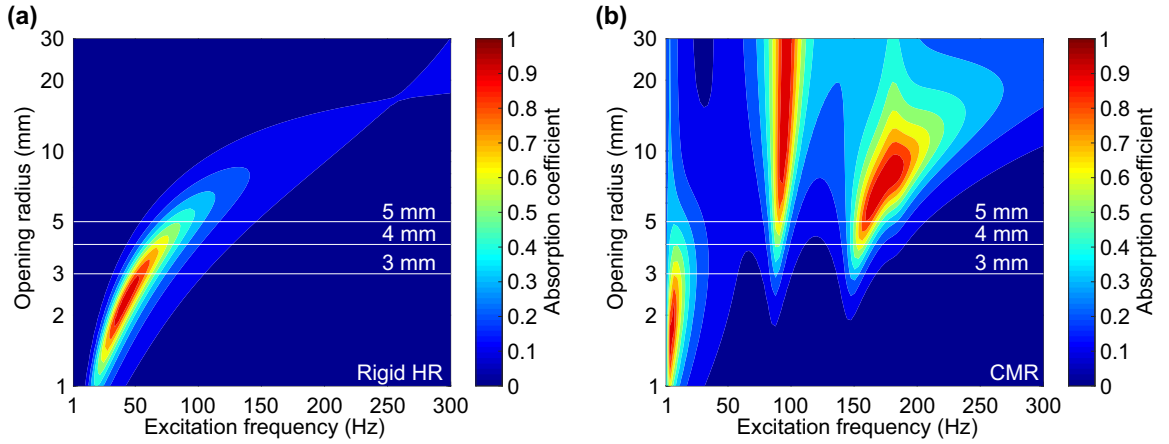

FIG. 2. Analytical absorption coefficients of (a) a rigid HR and (b) a CMR for 1–300 Hz and 1–30 mm opening radius. The side length of the cubic cavity is 11 cm, the neck length is 1.7 cm, and the wall thickness of the CMR is 10 mm.

For a specific opening radius, Fig. 2(a) shows that the rigid HR yields only one frequency where large sound absorption is achieved. Given the prescribed volume of the rigid HR, one opening radius maximizes the absorption coefficient, i.e., around 2.5 mm in Fig. 2(a). In contrast, for the CMR in Fig. 2(b), there are three local maxima of the absorption coefficient for this range of opening radii at frequencies less than 300 Hz. In addition, tuning the opening radius can tune the frequency of peak sound absorption while maintaining near-total sound absorption. For instance, two hybrid resonances with near-total sound absorption may be spectrally shifted within a frequency range of 80–200 Hz by changes in the opening radius from 5 to 12 mm. The large extent of coupling among the air motion in the CMR opening, the inner acoustic pressure in the cavity, and the structural displacement of the soft-material walls is the unique attribute that yields such intricate hybrid resonances.

Modeled as thin simply supported plates, the square walls of the CMR exhibit lowest-order symmetric modes with natural frequencies of 20, 101, and 181 Hz. The symmetric modes are strongly coupled to the acoustic field in the cavity, resulting in the distinct multiple low-frequency hybrid resonances observed in Fig. 2(b). For example, the large sound absorption at frequencies around 10 Hz seen for small opening radii in Fig. 2(b) is associated with a CMR motion analogous to the contraction and expansion of a balloon, according to the relative phases of the wall deflection, inner acoustic pressure, and motion of the air mass in the opening. In other words, the structural modes of the CMR walls activate strong coupling to the inner acoustic-pressure field and thus appear to magnify sound absorption to near-perfect levels. Similar conclusions may be reached regarding the hybrid resonances near 90 and 160 Hz for larger opening radii. Unlike a traditional rigid HR that relies on acoustic-impedance matching to absorb acoustic waves [29,38], the CMR appears to capitalize on strong coupling among multiple types of physics to exert tunable broadband control over the acoustic-energy transfer. This hypothesis is specifically tested and verified in Sec. IV.

The lines and labels in Fig. 2(b) identify the absorption coefficients of the CMR for opening radii of 5, 4, and 3 mm. For these opening radii, Fig. 3(a) presents experimental (markers) and analytical (curves) results for the absorption coefficient to validate the proposed concept of the CMR. In the frequency range 50–200 Hz, there are two local maxima of sound absorption for the CMR. With an increase in the opening radius, the amplitudes of the local maxima of the absorption coefficient increase, and the peaks shift to higher frequencies. The impedance of the CMR reveals the contributions from reciprocating energy (reactance) and dissipated energy (resistance), and the magnitude of the impedance. Figure 3(b) shows the experimental (markers) and analytical (curves) results for the components of the normalized specific acoustic impedance of a CMR with a 5 mm opening radius. There are two local minima in the impedance magnitude, occurring at frequencies where sound absorption is locally maximized for the case of a 5 mm opening radius shown in Fig. 3(a). The impedance-match method [14] eliminates the reactance and aims to match the resistance to the background media to achieve near-total absorption. Here, for the CMR, the local minimum in the magnitude of the impedance leads to high or near-total absorption. Rather than requiring subtle tuning of design parameters, the CMR permits a wide range of design to achieve such near-total absorption, as exemplified in Fig. 2(b). One benefit of the CMR is that high absorption is achieved over a wide frequency range, unlike the narrowband tuned sound absorption provided by traditional rigid HRs. For instance, the CMR has a broad 22 Hz bandwidth (full width at half maximum) of

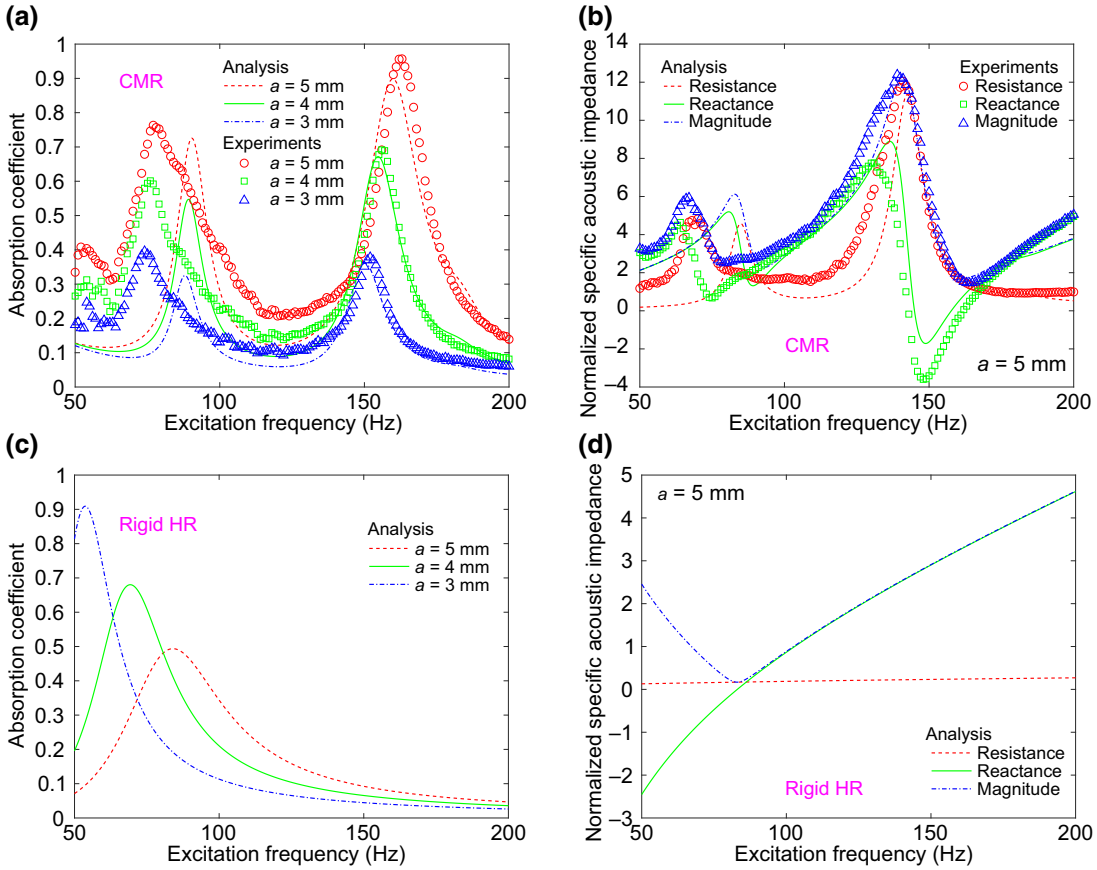

FIG. 3. (a) Analytical and experimental results for absorption coefficient of a CMR with opening radii of 5 mm (red dashed line and red circles), 4 mm (green solid line and green squares), and 3 mm (blue dotted-dash line and blue triangles) as a function of frequency from 50 to 200 Hz. (b) Analytical and experimental results for the resistance (red dash line and red circles), reactance (green solid line and green squares), and impedance magnitude (blue dotted-dash line and blue triangles) of a CMR with opening radius 5 mm. (c) Analytical results for absorption coefficient of a rigid HR (with the same volume as the CMR, and neck length 1.7 cm) with opening radii 5 mm (red dashed line), 4 mm (green solid line), and 3 mm (blue dotted-dash line). (d) Analytical results for the resistance (red dashed line), reactance (green solid line), and impedance magnitude (blue dotted-dash line) of a rigid HR with opening radius 5 mm.

the peak of sound absorption at 163 Hz for a 5 mm opening radius, as shown in Fig. 3(a). For the same physical dimensions as the CMR, a rigid HR with a 5 mm opening radius has one local maximum of sound absorption that is at most around $\alpha = 0.5$, as found in Fig. 2(a). There are also frequency shifts between the experimental and analytical results around the first sound absorption peak near 100 Hz in Fig. 3(b). These differences occur due to the relatively small-diameter opening between the CMR and the impedance tube, which may induce nonlinear aerodynamic behavior [39] resulting from the high particle velocity in the CMR neck.

To clarify the relations between impedance and absorption for a rigid-walled HR with the same volume and open-neck dimensions as the CMR, the analytical model is utilized to determine the absorption coefficients of a rigid HR shown in Figs. 3(c) and 3(d) for opening radii of 5 mm (red dashed lines), 4 mm (green solid lines), and 3 mm (blue dotted-dashed lines). For each opening radius shown in Fig. 3(c), there is one absorption-coefficient peak. With a decrease in the opening radius, the absorption-peak amplitude increases, and the peak frequency decreases. The resistance (red dashed line), reactance (green solid line), and impedance magnitude (blue dotted-dashed line) of the rigid HR with a 5 mm opening radius are shown in Fig. 3(d). The absorption-peak frequency (5 mm, red dashed line) in Fig. 3(c) corresponds to the frequency at which the reactance is zero and the impedance magnitude is minimized in Fig. 3(d), which is the definition of the conventional Helmholtz resonant frequency [29].

A similar correlation between absorption peaks and impedance-magnitude minimization is also observed in Figs. 3(a) and 3(b) for the CMR. For both the rigid HR and the CMR, the system resonance leads to absorption of sound. Yet the origins of the resonances are distinct. For the rigid HR, the resonance is singular and related to the lumped air mass and air spring exchanging kinetic and potential acoustic energy. For the CMR, hybrid resonances

of the wall, the inner pressure field, and the air mass in the opening result in an energy exchange among the structural strain and kinetic energy and the acoustic potential and kinetic energy that results in multiple-frequency absorption. These evaluations confirm the efficacy of the CMR for achieving low- and broadband-frequency sound absorption without relying on the addition of heavy masses or a complex material assembly. The results also reveal that impedance-magnitude minimization is the origin of the local maxima in sound absorption. Yet, the working mechanisms underlying these behaviors remain to be uncovered.

IV. MECHANISMS FOR NEAR-TOTAL ABSORPTION AT ARBITRARY FREQUENCY

Leveraging the analytical formulation derived to investigate the CMR, we explore the mechanisms that give rise to the near-total sound-absorption phenomenon. For a CMR having an inner side length of 5 cm, an opening radius of 3.1 mm, and a neck length of 1.7 cm, the absorption coefficients at 179 Hz are shown in Fig. 4(a) as a function of wall-material Young's modulus and wall thickness. For a rigid HR of the same physical dimensions, the Helmholtz resonance is at 180 Hz. Therefore Fig. 4(a) suggests a threshold of material and structural compliance for the CMR to respond similarly to a traditional rigid HR. It is observed that for smaller wall thicknesses such as 1 mm, the Young's modulus must increase substantially, e.g., to around 100 GPa, to cause near-total absorption. Yet for thicker walls, e.g., 10 mm, a smaller Young's modulus such as 100 MPa yields almost perfect sound absorption. This trend is due to the bending stiffness D of the compliant walls, where $D = Eh^3/[12(1-\nu^2)]$. Assuming Poisson's ratio ν remains the same, then the bending stiffness increases proportionally to Young's modulus E and increases according to the cube of the wall thickness h. These findings reveal that the structural dynamics of the compliant walls of the CMR introduce a coupling among the wall deflection, inner pressure field, and air motion in the opening. With less coupling among the components of the CMR caused by stiff and inflexible walls, the system responds similarly to a traditional rigid HR. A greater coupling among the degrees of freedom of the CMR creates subwavelength, broadband, and near-total absorption of sound.

A way to tailor the mechanical properties of the CMR walls so as to enable robust and near-total sound absorption is investigated. Here, the CMR has an inner side length of 11 cm, an opening radius of 9 mm, and a neck length of 1.7 cm. The results for sound absorption at 179 Hz are shown by the contour color shading in Fig. 4(b). With the same cavity and opening dimensions, the rigid HR exhibits a Helmholtz resonance at 133 Hz. Yet, by strategic selection of the wall-material modulus and thickness, the CMR achieves near-total absorption at the target frequency of 179 Hz, shown by the darker red color in Fig. 4(b) for the larger wall thickness and smaller Young's modulus. This is enabled despite the fact that the counterpart rigid HR provides nearly no sound absorption at this frequency, since 179 Hz is well off the resonance at 133 Hz. As uncovered through additional studies presented in Appendices C and D, the wall thickness and Young's modulus can individually be used to tune the sound-absorption characteristics of the CMR in still more nuanced ways.

To contrast the use of a rigid HR and a CMR for near-total absorption at 179 Hz, Fig. 4(c) provides an analytical and experimental examination. To construct the rigid HR, acrylic PMMA [thickness 6.35 mm and Young's modulus 3.2 GPa, highlighted by the star marker in Fig. 4(a)] is used to fabricate the cavity walls. Since the same Helmholtz resonance would be achieved by another rigid HR with a larger volume and a larger opening, the size of the HR is not an influencing factor in this comparison. In addition,

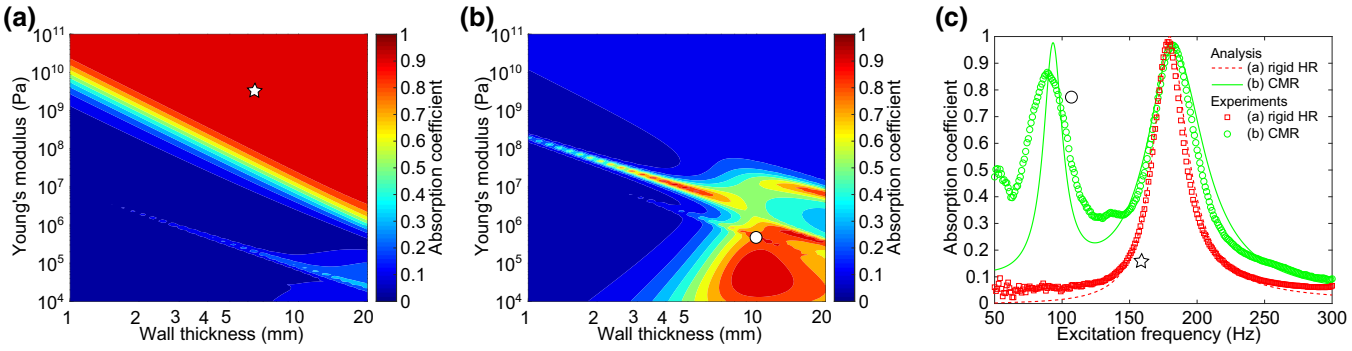

FIG. 4. Analytical absorption coefficients at 179 Hz for a CMR of (a) inner side length 5 cm, opening radius 3.1 mm, and neck length 1.7 cm, and (b) inner side length 11 cm, opening radius 9 mm, and neck length 1.7 cm, as a function of wall-material Young's modulus and wall thickness. (c) Absorption coefficients of the two CMRs selected in (a) and (b), marked by a star and a circle, respectively, as a function of frequency from 50 to 300 Hz. Results for (a) are denoted by a red dashed line (analytical) and red squares (experimental), and results for (b) are denoted by a green solid line (analytical) and green circles (experimental).

the absorption capabilities of a rigid HR and a CMR of the same net size are compared and discussed in Sec. III. Here, the CMR has a wall thickness of 10 mm and a Young's modulus of 0.5 MPa, highlighted by the circle in Fig. 4(b). The analytical (red dashed and green solid lines) and experimental (red squares and green circles) results for the absorption coefficient of the rigid HR and the CMR are presented in Fig. 4(c). The rigid HR has one frequency of near-total sound absorption at 179 Hz and nearly no sound absorption off resonance. Yet, for the CMR, near-total sound absorption is achieved at 179 Hz as well as at 90 Hz, a far more subwavelength response than that delivered by the rigid HR. In fact, the hybrid resonances provided by the CMR are both more broadband in sound absorption than that of the rigid HR. With the CMR, hybrid resonances can be achieved at desired frequencies, with the design parameters acquired from the model created here. The rich multiphysics coupling among materials science, structural dynamics, and acoustics enables a simple monolithic-material design to substantially control acoustic-energy transfer and dissipation using lightweight soft materials.

V. CONCLUSIONS

The hybrid resonances manifested in the compliant-material resonator enable multiple-frequency absorption, while the material compliance of the cavity walls increases the frequency bandwidth of the sound absorption. The subwavelength dimensions of the compliant-material resonator and its straightforward structure enable simple fabrication and tuning strategies for versatile implementation. The compliant-material resonator can be applied for extremely low-frequency sound attenuation [4], and may be integrated into existing barriers for greater energy control [40]. The concept of utilizing multiphysics coupling to introduce hybrid resonances may be leveraged to design classes of acoustic-energy-transfer and energy-harvesting devices [41,42], and may potentially inspire designs of active sound absorbers [43–45].

ACKNOWLEDGMENTS

The authors are grateful to the Ford Motor Company for partially supporting this work.

APPENDIX A: ANALYTICAL MODELING OF THE COMPLIANT-MATERIAL RESONATOR

Because of the low frequency range of interest in this study and the relatively small dimensions of the CMR, a long-wavelength approximation is used in the modeling. The walls of the CMR are modeled as simply supported thin plates [46]. The air in the neck is assumed to be a lumped mass moving uniformly across the opening area [29]. The behavior of the CMR is the outcome of the effect of coupling of the deflection of the compliant walls w, the inner pressure field p, and the displacement of the lumped air mass in the opening ξ. The coupling between the inner pressure field and the compliant walls is developed referencing the analysis conducted by Dowell *et al.* [47]. The inner pressure field satisfies the classical wave equation

$$\nabla^2 p - \frac{1}{c_0^2}\frac{\partial^2 p}{\partial t^2} = 0, \tag{A1}$$

where c_0 is the sound speed in air, and t denotes the time. The coupling between the pressure field and the wall deflection on a flexible wall of area A_F is expressed as

$$\frac{\partial p}{\partial n} = -\rho_0 \frac{\partial^2 w}{\partial t^2}, \tag{A2}$$

where n is the normal direction (positive outward) and ρ_0 is the air density. The absorbing influence of the material for an absorbent wall of area A_A is also taken into consideration by

$$\frac{\partial p}{\partial n} = -\rho_0 \frac{\dot{p}}{z_A}, \tag{A3}$$

where z_A is the material impedance and the overdot denotes the derivative with respect to time. The coupling between the pressure field and the motion of the lumped air in the opening (of area A_{HR}) is achieved as follows:

$$\frac{\partial p}{\partial n} = -\rho_0 \frac{d^2 \xi}{dt^2}. \tag{A4}$$

For the inner pressure field, we assume that the rigid-wall normal modes F_n have the following properties:

$$\nabla^2 F_n = -\frac{\omega_{An}^2}{c_0^2} F_n, \tag{A5}$$

$$\frac{\partial F_n}{\partial n} = 0, \tag{A6}$$

$$\frac{1}{V}\int_V F_n^2 \, dv = M_n^A, \tag{A7}$$

where ω_{An} are the natural frequencies associated with the rigid-wall normal modes F_n. The following terms are defined:

$$P_n = \frac{1}{\rho_0 c_0^2 V}\int_V p F_n \, dv, \tag{A8}$$

$$W_n = \frac{1}{A_F}\int_{A_F} w F_n \, dA, \tag{A9}$$

$$C_{nr} = \frac{1}{A_A}\int_{A_A} \frac{F_n F_r}{z_A} \, dA, \tag{A10}$$

where V is the total volume of the cavity. Then the pressure field p is expressed as the summation of all modes:

$$p = \rho_0 c_0^2 \sum_n (P_n / M_n^A) F_n. \tag{A11}$$

To obtain the ordinary differential equation (ODE) for the acoustic modes, Green's theorem is applied in the form

$$\int_v (p \nabla^2 F_n - F_n \nabla^2 p)\, dv = \int_A \left(p \frac{\partial F_n}{\partial n} - F_n \frac{\partial p}{\partial n} \right) dA. \tag{A12}$$

By substituting Eqs. (A1)–(A11) into Eq. (A12), the ODE set for the pressure field is arrived at:

$$\ddot{P}_n + \omega_{An}^2 P_n + \frac{A_A}{V} \rho_0 c_0^2 \sum_r \frac{\dot{P}_r C_{nr}}{M_r^A} = -\frac{A_F}{V} \ddot{W}_n - \frac{1}{V} \ddot{\xi} \int_{A_{\mathrm{HR}}} F_n\, dA. \tag{A13}$$

Similarly, the wall deflection w is also expressed as the summation of all modes:

$$w = \sum_m q_m \Psi_m, \tag{A14}$$

where Ψ_m is the mth mode shape and q_m is the generalized coordinate associated with it. By substituting Eq. (A14) into Eq. (A9), the term W_n is then expressed by the wall modes as

$$W_n = \sum_m \frac{1}{A_F} \int_{A_F} q_m \Psi_m F_n\, dA. \tag{A15}$$

To relate the wall modes and the acoustic modes, a coupling term is derived as follows:

$$L_{nm} = \frac{1}{A_F} \int_{A_F} F_n \Psi_m\, dA. \tag{A16}$$

Then W_n is expressed as

$$W_n = \sum_m L_{nm} q_m. \tag{A17}$$

By substituting Eq. (A17) into Eq. (A13), one gets the governing equation for the inner pressure field,

$$\ddot{P}_n + \omega_{An}^2 P_n + \frac{A_A}{V} \rho_0 c_0^2 \sum_r \frac{\dot{P}_r C_{nr}}{M_r^A} = -\sum_m \frac{A_F}{V} L_{nm} \ddot{q}_m - \frac{1}{V} \ddot{\xi} \int_{A_{\mathrm{HR}}} F_n\, dA.$$

After obtaining the governing equation for the acoustic pressure inside the cavity, the wall deflection is analyzed. Considering the wall as a thin plate that is excited by the inner pressure field, the governing equation for the wall deflection w is achieved as

$$D \nabla^4 w + m_w \frac{\partial^2 w}{\partial t^2} = p. \tag{A18}$$

Here $D = (Eh^3/12(1-\nu^2))$ is the bending stiffness determined by the material Young's modulus E, Poisson's ratio ν, and the wall thickness h, and m_w is the density per unit area. The mode shapes Ψ_m of the wall are orthogonal, and satisfy the equation

$$D \nabla^4 \Psi_m - m_w \omega_m^2 \Psi_m = 0. \tag{A19}$$

Because of the infinitesimal acoustic pressures involved that couple to the walls, the boundary conditions on the walls are assumed to be simple support on all edges, and then the natural frequency ω_m is

$$\omega_m = \pi^2 \left(\frac{i^2}{b^2} + \frac{j^2}{b^2} \right) \sqrt{\frac{D}{m_w}}, \tag{A20}$$

where the numbers of the nodal lines for the mth mode are $i-1$ and $j-1$, respectively, in two directions on the square wall.

By substituting Eqs. (A14) and (A19) into Eq. (A18), the governing equation for the generalized coordinates is obtained as

$$\sum_m m_w (\ddot{q}_m + \omega_m^2 q_m) \Psi_m = p. \tag{A21}$$

To simplify Eq. (A21), the orthogonality condition on the mode shapes is applied. We multiply Eq. (A21) by another mode shape and integrate over the area of the flexible wall, and then the governing equation for q_m is achieved as follows:

$$(\ddot{q}_m + \omega_m^2 q_m) \int_{A_F} m_w \Psi_m^2\, dA = \int_{A_F} \Psi_m p\, dA. \tag{A22}$$

To simplify the governing equation Eq. (A22), the orthogonality condition is expressed as

$$\int_{A_F} m_w \Psi_m^2\, dA = D_w. \tag{A23}$$

Equations (A11) and (A16) are then substituted into Eq. (A21) to get the governing equation

$$D_w (\ddot{q}_m + \omega_m^2 q_m) = \rho_0 c_0^2 A_F \sum_n \frac{P_n L_{nm}}{M_n^A}.$$

Then, for the lumped mass in the opening, a force balance is applied to characterize the air-mass motion. By balancing the forces on both sides of the opening, the governing

equation for the air motion is obtained as follows:

$$m\ddot{\xi} + R\dot{\xi} = A_{\mathrm{HR}}p + A_{\mathrm{HR}}Pe^{j\omega t}. \tag{A24}$$

In Eq. (A24), $m = \rho_0 A_{\mathrm{HR}} L'$ is the equivalent air mass in the opening, $L' = L + 1.7a$ is the end-corrected neck length for a neck of length L and opening radius a [47], R is the sum of the radiation resistance and thermoviscous resistance for the opening [29], and $Pe^{j\omega t}$ is the harmonic plane wave excitation. By substituting the expression for the inner pressure field, Eq. (A11), into Eq. (A24), the governing equation for the air-mass motion in the opening is expressed as

$$m\ddot{\xi} + R\dot{\xi} = A_{\mathrm{HR}}\rho_0 c_0^2 \sum_n \frac{P_n F_n}{M_n^A} + A_{\mathrm{HR}}Pe^{j\omega t}.$$

The governing equations for the compliant-material resonator are given all together by Eqs. (1)–(3). In order to study the behavior of the CMR compared with a traditional rigid HR, the specific acoustic impedance and absorption coefficient are determined by solving the governing equations derived above. The specific acoustic impedance is the ratio of acoustic pressure to fluid particle velocity. In this paper, due to the low frequency range of interest, we consider only the zeroth-order mode of the inner pressure field, where $\omega_{A0} = 0$ and $M_0^A = 1$ [48]. In addition, only the odd modes of the wall are considered, because the even modes do not appreciably contribute to changes in the acoustic pressure in the cavity [49]. In this study, the 1·1, 1·3, 3·1, and 3·3 modes are considered, where the numbers of nodal lines for the mode shapes are 0 and 0, 0 and 2, 2 and 0, and 2 and 2, respectively. The 1·3 and 3·1 modes have the same natural frequencies and generalized-coordinate responses owing to the square shape of the wall. Therefore, only the response of the 1·3 mode is calculated, and the influence is doubled in the coupling term with the inner pressure. Taking these strategies into account, the governing equations are Eqs. (A25)–(A29):

$$\ddot{P}_0 + \omega_{A0}^2 P_0 + \frac{\rho_0 c_0}{z_A}\frac{A_A c_0}{V M_0^A}\dot{P}_0 = -\frac{A_F}{V}L_{01}\ddot{q}_1 - \frac{2A_F}{V}L_{02}\ddot{q}_2 - \frac{A_F}{V}L_{03}\ddot{q}_3 - \frac{A_{\mathrm{HR}}}{V}\ddot{\xi}, \tag{A25}$$

$$\ddot{q}_{11} + \omega_{11}^2 q_{11} = \frac{\rho_0 c_0^2 A_F L_{01}}{M_0^A D_w}P_0, \tag{A26}$$

$$\ddot{q}_{13} + \omega_{13}^2 q_{13} = \frac{\rho_0 c_0^2 A_F L_{02}}{M_0^A D_w}P_0, \tag{A27}$$

$$\ddot{q}_{33} + \omega_{33}^2 q_{33} = \frac{\rho_0 c_0^2 A_F L_{03}}{M_0^A D_w}P_0, \tag{A28}$$

$$m\ddot{\xi} + R\dot{\xi} = \frac{A_{\mathrm{HR}}\rho_0 c_0^2}{M_0^A}P_0 + A_{\mathrm{HR}}Pe^{j\omega t}. \tag{A29}$$

Further simplification of the governing equations is achieved by defining the following coefficients:

$$\sigma = \frac{\rho_0 c_0}{z_A}\frac{A_A c_0}{V M_0^A},\ \delta_1 = \frac{A_F}{V}L_{01},\ \delta_2 = \frac{2A_F}{V}L_{02},\ \delta_3 = \frac{A_F}{V}L_{03},$$

$$\kappa = \frac{A_{\mathrm{HR}}}{V},$$

$$\zeta_1 = \frac{\rho_0 c_0^2 A_F L_{01}}{M_0^A D_w},\ \zeta_2 = \frac{\rho_0 c_0^2 A_F L_{02}}{M_0^A D_w},\ \zeta_3 = \frac{\rho_0 c_0^2 A_F L_{03}}{M_0^A D_w},$$

$$\varphi = \frac{A_{\mathrm{HR}}\rho_0 c_0^2}{M_0^A}.$$

By substituting the above constants and recalling that $\omega_{A0} = 0$, the governing Eqs. (A25)–(A29) are expressed as

$$\ddot{P}_0 + \sigma\dot{P}_0 = -\delta_1\ddot{q}_1 - \delta_2\ddot{q}_2 - \delta_3\ddot{q}_3 - \kappa\ddot{\xi}, \tag{A30}$$

$$\ddot{q}_{11} + \omega_{11}^2 q_{11} = \zeta_1 P_0, \tag{A31}$$

$$\ddot{q}_{13} + \omega_{13}^2 q_{13} = \zeta_2 P_0, \tag{A32}$$

$$\ddot{q}_{33} + \omega_{33}^2 q_{33} = \zeta_3 P_0, \tag{A33}$$

$$m\ddot{\xi} + R\dot{\xi} = \varphi P_0 + A_{\mathrm{HR}}Pe^{j\omega t}. \tag{A34}$$

In order to obtain the absorption coefficient of the CMR, the specific acoustic impedance of the CMR is first derived. The specific acoustic impedance at the opening of the CMR is the ratio of the excitation pressure amplitude to the particle velocity of the lumped air in the opening. Harmonic responses are assumed, and Eqs. (A30)–(A34) are expressed in terms of P_0, q_{ij}, and $\dot{\xi}$. Then, by substituting Eqs. (A30)–(A33) into Eq. (A34), the impedance at the opening is obtained as

$$Z_{\mathrm{opening}} = \frac{P}{\dot{\xi}} = \left(j\omega m + R + \frac{j\omega\kappa\varphi}{-\omega^2 + j\omega\sigma - [\omega^2\delta_1\zeta_1/(-\omega^2+\omega_{11}^2)] - [\omega^2\delta_2\zeta_2/(-\omega^2+\omega_{13}^2)] - (\omega^2\delta_3\zeta_3/(-\omega^2+\omega_{33}^2))}\right)/A_{\mathrm{HR}}, \tag{A35}$$

where $\dot{\xi}$ is the complex amplitude of $\dot{\xi}$, and ω is the harmonic plane wave excitation frequency. The total normalized specific acoustic impedance of the CMR is then found to be

$$\frac{Z}{Z_0} = \frac{A_{\text{tube}}}{A_{\text{HR}}} \frac{Z_{\text{opening}}}{\rho_0 c_0}, \tag{A36}$$

where A_{tube} is the cross-section area of the impedance tube, and $Z_0 = \rho_0 c_0$ is the specific acoustic impedance of air. Then the absorption coefficient of the CMR, α, is expressed as presented in the text in Eq. (4), repeated here for completeness:

$$\alpha = 1 - \left| \frac{Z/Z_0 - 1}{Z/Z_0 + 1} \right|^2.$$

APPENDIX B: EXPERIMENTAL FABRICATION AND METHODS

The compliant-material resonator is fabricated by casting silicone rubber (Smooth-on, Inc., Mold Star 15s) into a mold that is the negative of the CMR. The necks for tuning the opening radius are fabricated by 3D printing of ABS plastic (FlashForge Creator Pro). The measurements of the absorption coefficients and impedances in Figs. 3 and 4(c) are conducted in an impedance tube with a 76.2 mm interior diameter in accordance with ASTM E1050-12. Instead of the specimen being mounted inside the end of the impedance tube, the CMR is mounted on the side of the tube, at the end of the tube. The CMR is connected to the tube by a 3D printed neck. A speaker is mounted on one end of the impedance tube, and a rigid termination of the impedance tube at the CMR end is applied. Two microphones (PCB 130E20) are mounted on the tube to measure the complex acoustic pressure. White noise is generated by the data-processing computer and fed through a power amplifier (AudioSource AMP 100) to the speaker. A signal conditioner (PCB 482C05) and a National Instruments data acquisition system (NI 6341) are applied to send the measured data to MATLAB for postprocessing. The absorption coefficient and the normalized specific acoustic impedance can then be obtained from the complex transfer function measured by the two microphones. The experimental setup for the impedance-tube tests is presented in Fig. 5.

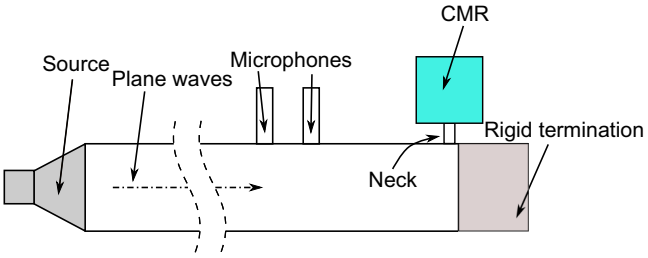

FIG. 5. Experimental setup for impedance tube.

APPENDIX C: WALL THICKNESS FOR TUNING STRUCTURAL COMPLIANCE OF THE CMR

In the main text, the parameter selection of the combination of Young's modulus and wall thickness to achieve near-total absorption in a CMR is investigated. Here the significance of the Young's modulus and the wall thickness individually is illuminated. First a CMR with a thinner wall is investigated. The thinner CMR has an inner side length of 10 cm and a wall thickness of 5 mm, and is fabricated from the same material as that in Fig. 3 with properties Young's modulus 0.5 MPa, Poisson's ratio 0.49, and density 1145 kg/m^3. Figure 6 presents the experimental (markers) and analytical (lines) results for the absorption coefficient of thinner CMRs with opening radii 5, 4, and 3 mm from 50 to 300 Hz.

In Fig. 6, at frequencies around 60 Hz and around 200 Hz, absorption-coefficient peaks are observed. In addition, increasing the opening radius enables sound absorption closer to near-total absorption, and causes a slight shift to higher frequency in the peak around 200 Hz, which is evident from comparing the results for increased opening radius in Fig. 6. Although the overall trends in the absorption coefficient for the thinner CMR are analogous to those for the 10-mm-thick CMR presented in Fig. 3(a), the near-total absorptions occur at distinct frequencies. The absorption peaks in Fig. 6 occur at around 60 and 200 Hz, and the near-total absorptions in Fig. 3(a) are at around 90 and 160 Hz. The difference in absorption-peak frequencies between the CMRs with thinner and thicker walls indicates

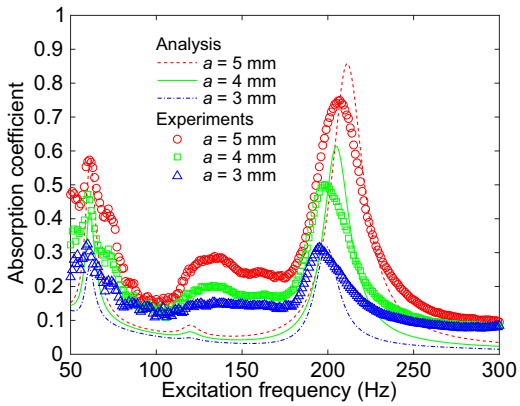

FIG. 6. Analytical and experimental results for absorption coefficients of CMRs of opening radii 5 mm (red dashed line and red circles), 4 mm (green solid line and green squares), and 3 mm (blue dotted-dashed line and blue triangles). The CMR has a cubic cavity of side length 10 cm, a wall thickness of 5 mm, and a neck length of 1.7 cm.

that the wall thickness has an influence on the absorption characteristics of a CMR.

To compare the influence of the wall thickness on the absorption characteristics of a rigid HR and a CMR, an analytical study is conducted. Figure 7 presents the absorption coefficients of a rigid HR [Fig. 7(a)] and a CMR [Fig. 7(b)] for wall thicknesses of 3, 5, 7, and 9 mm. For both the rigid HR and the CMR, the inner side length of the cubic cavity is 11 cm, the opening radius is 5 mm, and the neck length is the same as the wall thickness. As presented in Fig. 7(a), the rigid HR has one absorption-coefficient peak for each wall thickness, and the peak amplitudes are less than 0.5. For the CMR as shown in Fig. 7(b), there are two major absorption peaks (with absorption coefficient greater than 0.5) for all four wall thicknesses. With an increase in wall thickness, the two major peaks shift towards the middle frequency. Yet the two major peaks for each wall thickness presented in Fig. 7(b) are associated with distinct modes of the wall. The natural frequencies of the 1·3 and 3·1 modes are 30.2, 50.3, 70.4, and 90.5 Hz for the 3, 5, 7, and 9 mm walls, respectively, which correspond to the absorption-peak frequencies in Fig. 7(b) for each wall thickness. The near-total absorption around 175, 190, 220, and 270 Hz for the four wall thicknesses is the outcome of the hybrid effect of the wall compliance and the zero mode of the pressure field (Helmholtz mode). For smaller wall thicknesses, the wall compliance softens the rigid HR significantly and thus decreases the equivalent stiffness of the HR. With decreased stiffness and unchanged mass in the open neck, the resonant frequency is increased, as can be seen by comparing the near-total absorption of the CMR in Fig. 7(b) with the peak for the same wall thickness for the rigid HR in Fig. 7(a). By contrasting the four near-total absorptions (from 150 to 300 Hz) in Fig. 7(b), it is observed that increasing the wall thickness lessens the softening effect, and thus lowers the resonant frequency. By adjusting the wall thickness, tuning of the structural compliance of the CMR and multiple-frequency near-total absorption are achieved, compared with the rigid HR.

APPENDIX D: MATERIAL COMPLIANCE FOR MULTIPLE-FREQUENCY AND NEAR-TOTAL ABSORPTION

An investigation of the influence of the Young's modulus on the absorption characteristics of a CMR is conducted. Figure 8 presents the analytical absorption coefficients of a CMR for 1–300 Hz and a Young's modulus from 10 kPa to 10 GPa. The inner-cavity side length of the CMR is 11 cm, the opening radius is 5 mm, the wall thickness is 10 mm, and the neck length is 2 cm. Shown at the top of Fig. 8 are absorption coefficients for a rigid HR with the same geometric parameters, with a Helmholtz resonance at 79 Hz. As presented in Fig. 8, for the CMR, for a large Young's modulus such as one greater than 1 GPa, the absorption coefficients are nearly the same as those of the rigid HR. When the Young's modulus is smaller, such as around 1 MPa, multiple-frequency absorption occurs, and near-total absorption is also achieved as indicated by the dark red color. In addition, by tuning the Young's modulus of the wall material, absorption at either a lower or a higher frequency compared with the rigid HR can be realized. Traditionally, in order to achieve low-frequency sound absorption, a rigid HR needs to have large geometric dimensions, even for coiled-up resonators. Yet, by decreasing the Young's modulus of the wall material, in other words by utilizing softer materials, greater sound absorption at subwavelength frequency can be achieved. The multiple-low-frequency and near-total absorption is realized by strong coupling of the structural response, acoustic-pressure field, and air motion in the

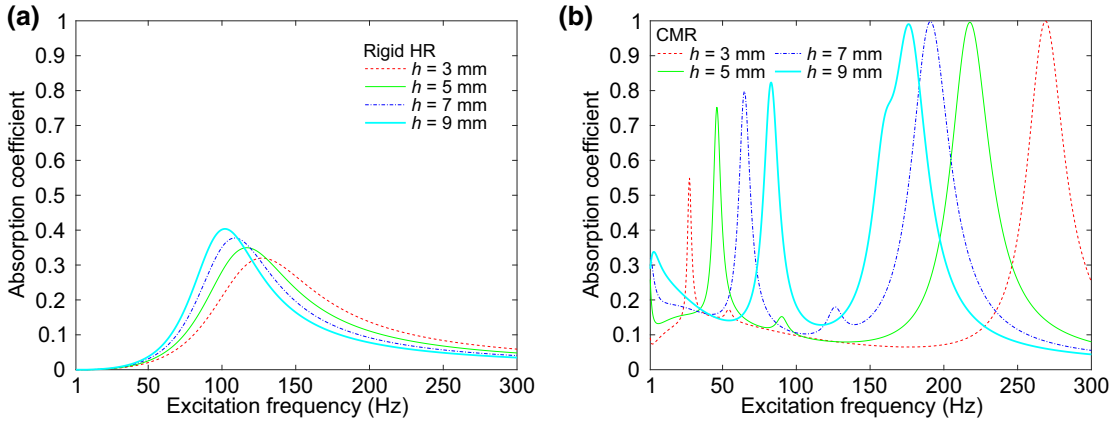

FIG. 7. Analytical absorption coefficients of (a) a rigid HR and (b) a CMR as a function of frequency from 1 to 300 Hz and wall thicknesses 3 mm (red dashed line), 5 mm (green solid line), 7 mm (blue dotted-dashed line), and 9 mm (thick cyan solid line). Both the CMR and the HR have a cubic cavity of side length 11 cm and opening radius 5 mm. The neck length is the same as the corresponding wall thickness.

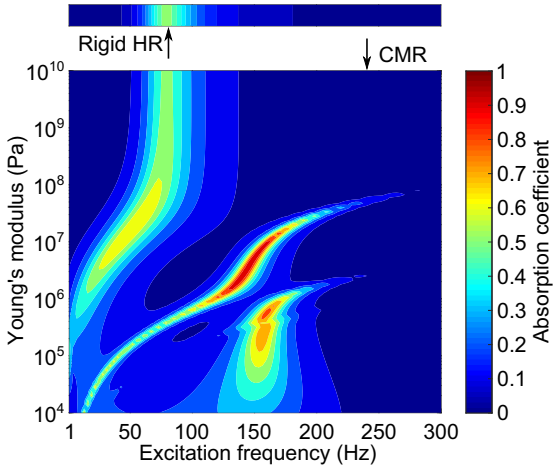

FIG. 8. Analytical absorption coefficients of a CMR as a function of frequency from 1 to 300 Hz and for a Young's modulus from 10 kPa to 10 GPa. The side length of the cubic cavity of the CMR is 11 cm, the opening radius is 5 mm, the wall thickness is 10 mm, and the neck length is 2 cm. The analytical absorption coefficients of a rigid HR with the same geometric parameters are presented at the top of the contour plot.

opening through the material compliance. The compliant-material resonator enables multiphysics coupling, hybrid resonances, and impedance tuning for greater control of acoustic energy. Such discoveries greatly contribute to the study of techniques for acoustic-energy attenuation and may inspire future investigations of sound-absorption devices.

[1] F. Lemoult, N. Kaina, M. Fink, and G. Lerosey, Wave propagation control at the deep subwavelength scale in metamaterials, Nat. Phys. **9**, 55 (2013).

[2] T. Brunet, A. Merlin, B. Mascaro, K. Zimny, J. Leng, O. Poncelet, C. Aristégui, and O. Mondain-Monval, Soft 3D acoustic metamaterial with negative index, Nat. Mater. **14**, 384 (2015).

[3] C. Fu, X. Zhang, M. Yang, S. Xiao, and Z. Yang, Hybrid membrane resonators for multiple frequency asymmetric absorption and reflection in large waveguide, Appl. Phys. Lett. **110**, 021901 (2017).

[4] A. Merkel, G. Theocharis, O. Richoux, V. Romero-García, and V. Pagneux, Control of acoustic absorption in one-dimensional scattering by resonant scatterers, Appl. Phys. Lett. **107**, 244102 (2015).

[5] Y. Lai, Y. Wu, P. Sheng, and Z. Zhang, Hybrid elastic solids, Nat. Mater. **10**, 620 (2011).

[6] N. Fang, D. Xi, J. Xu, M. Ambati, W. Srituravanich, C. Sun, and X. Zhang, Ultrasonic metamaterials with negative modulus, Nat. Mater. **5**, 452 (2006).

[7] A. Sanada and N. Tanaka, Extension of the frequency range of resonant sound absorbers using two-degree-of-freedom Helmholtz-based resonators with a flexible panel, Appl. Acoust. **74**, 509 (2013).

[8] G. Ma, M. Yang, S. Xiao, Z. Yang, and P. Sheng, Acoustic metasurface with hybrid resonances, Nat. Mater. **13**, 873 (2014).

[9] Y. Li and B. M. Assouar, Acoustic metasurface-based perfect absorber with deep subwavelength thickness, Appl. Phys. Lett. **108**, 063502 (2016).

[10] Y. Xie, W. Wang, H. Chen, A. Konneker, B. I. Popa, and S. A. Cummer, Wavefront modulation and subwavelength diffractive acoustics with an acoustic metasurface, Nat. Commun. **5**, 5553 (2014).

[11] J. Li, W. Wang, Y. Xie, B. I. Popa, and S. A. Cummer, A sound absorbing metasurface with coupled resonators, Appl. Phys. Lett. **109**, 091908 (2016).

[12] Y. Li, B. Liang, Z. M. Gu, X. Y. Zou, and J. C. Cheng, Reflected wavefront manipulation based on ultrathin planar acoustic metasurfaces, Sci. Rep. **3**, srep02546 (2013).

[13] Y. Li, X. Jiang, R. Q. Li, B. Liang, X. Y. Zou, L. L. Yin, and J. C. Cheng, Experimental Realization of Full Control of Reflected Waves with Subwavelength Acoustic Metasurfaces, Phys. Rev. Appl. **2**, 064002 (2014).

[14] Z. Yang, H. M. Dai, N. H. Chan, G. C. Ma, and P. Sheng, Acoustic metamaterial panels for sound attenuation in the 50–1000 Hz regime, Appl. Phys. Lett. **96**, 041906 (2010).

[15] X. N. Liu, G. K. Hu, G. L. Huang, and C. T. Sun, An elastic metamaterial with simultaneously negative mass density and bulk modulus, Appl. Phys. Lett. **98**, 251907 (2011).

[16] H. Long, Y. Cheng, J. Tao, and X. Liu, Perfect absorption of low-frequency sound waves by critically coupled subwavelength resonant system, Appl. Phys. Lett. **110**, 023502 (2017).

[17] V. Romero-García, G. Theocharis, O. Richoux, and V. Pagneux, Use of complex frequency plane to design broadband and sub-wavelength absorbers, J. Acoust. Soc. Am. **139**, 3395 (2016).

[18] J.-P. Groby, R. Pommier, and Y. Aurégan, Use of slow sound to design perfect and broadband passive sound absorbing materials, J. Acoust. Soc. Am. **139**, 1660 (2016).

[19] X. Cai, Q. Guo, G. Hu, and J. Yang, Ultrathin low-frequency sound absorbing panels based on coplanar spiral tubes or coplanar Helmholtz resonators, Appl. Phys. Lett. **105**, 121901 (2014).

[20] Y. Cheng, C. Zhou, B. G. Yuan, D. J. Wu, Q. Wei, and X. J. Liu, Ultra-sparse metasurface for high reflection of low-frequency sound based on artificial Mie resonances, Nat. Mater. **14**, 1013 (2015).

[21] L. Fok and X. Zhang, Negative acoustic index metamaterial, Phys. Rev. B **83**, 214304 (2011).

[22] S. H. Lee, C. M. Park, Y. M. Seo, Z. G. Wang, and C. K. Kim, Composite Acoustic Medium with Simultaneously Negative Density and Modulus, Phys. Rev. Lett. **104**, 054301 (2010).

[23] L. Fok, M. Ambati, and X. Zhang, Acoustic metamaterials, MRS Bull. **33**, 931 (2008).

[24] Y. Xie, B. I. Popa, L. Zigoneanu, and S. A. Cummer, Measurement of a Broadband Negative Index with Space-Coiling Acoustic Metamaterials, Phys. Rev. Lett. **110**, 175501 (2013).

[25] S. H. Mousavi, A. B. Khanikaev, and Z. Wang, Topologically protected elastic waves in phononic metamaterials, Nat. Commun. **6**, 8682 (2015).

[26] M. Yang, G. Ma, Z. Yang, and P. Sheng, Coupled Membranes with Doubly Negative Mass Density and Bulk Modulus, Phys. Rev. Lett. **110**, 134301 (2013).
[27] C. Zhang and X. Hu, Three-Dimensional Single-Port Labyrinthine Acoustic Metamaterial: Perfect Absorption with Large Bandwidth and Tunability, Phys. Rev. Appl. **6**, 064025 (2016).
[28] C. Shen, J. Xu, N. X. Fang, and Y. Jing, Anisotropic Complementary Acoustic Metamaterial for Canceling out Aberrating Layers, Phys. Rev. X **4**, 041033 (2014).
[29] L. E. Kinsler, A. R. Frey, A. B. Coppens, and J. V. Sanders, *Fundamentals of Acoustics* (John Wiley and Sons, New York, 2000).
[30] B. I. Popa and S. A. Cummer, Non-reciprocal and highly nonlinear active acoustic metamaterials, Nat. Commun. **5**, 3398 (2014).
[31] F. Ma, J. H. Wu, M. Huang, W. Zhang, and S. Zhang, A purely flexible lightweight membrane-type acoustic metamaterial, J. Phys. D: Appl. Phys. **48**, 175105 (2015).
[32] M. Yang, C. Meng, C. Fu, Y. Li, Z. Yang, and P. Sheng, Subwavelength total acoustic absorption with degenerate resonators, Appl. Phys. Lett. **107**, 104104 (2015).
[33] D. T. Blackstock, *Fundamentals of Physical Acoustics* (Wiley, New York, 2000).
[34] H. L. Zhang, Y. F. Zhu, B. Liang, J. Yang, J. Yang, and J. C. Cheng, Omnidirectional ventilated acoustic barrier, Appl. Phys. Lett. **111**, 203502 (2017).
[35] S. Qi, Y. Li, and B. Assouar, Acoustic Focusing and Energy Confinement Based on Multilateral Metasurfaces, Phys. Rev. Appl. **7**, 054006 (2017).
[36] Z. Zhou, W. Qin, and P. Zhu, Harvesting acoustic energy by coherence resonance of a bi-stable piezoelectric harvester, Energy **126**, 527 (2017).
[37] R. Fleury, D. L. Sounas, C. F. Sieck, M. R. Haberman, and A. Alù, Sound isolation and giant linear nonreciprocity in a compact acoustic circulator, Science **343**, 516 (2014).
[38] H. Lissek, E. Rivet, T. Laurence, and R. Fleury, Toward wideband steerable acoustic metasurfaces with arrays of active electroacoustic resonators, J. Appl. Phys. **123**, 091714 (2018).
[39] B. I. Popa, L. Zigoneanu, and S. A. Cummer, Tunable active acoustic metamaterials, Phys. Rev. B **88**, 024303 (2013).
[40] A. N. Norris and G. Wickham, Elastic Helmholtz resonators, J. Acoust. Soc. Am. **93**, 617 (1993).
[41] B. Assouar, B. Liang, Y. Wu, Y. Li, J. C. Cheng, and Y. Jing, Acoustic metasurfaces, Nat. Rev. Mater. **3**, 460 (2018).
[42] S. A. Cummer, J. Christensen, and A. Alù, Controlling sound with acoustic, Nat. Rev. Mater. **1**, 16001 (2016).
[43] D. M. Photiadis, The effect of wall elasticity on the properties of a Helmholtz resonator, J. Acoust. Soc. Am. **90**, 1188 (1991).
[44] S. Griffiths, B. Nennig, and S. Job, Porogranular materials composed of elastic Helmholtz resonators for acoustic wave, J. Acoust. Soc. Am. **141**, 254 (2017).
[45] G. K. Yu, Nonlinear amplitude-frequency response of a Helmholtz resonator, J. Vib. Acoust. **133**, 024502 (2011).
[46] A. W. Leissa, The free vibration of rectangular plates, J. Sound Vib. **31**, 257 (1973).
[47] E. H. Dowell, G. F. Gorman, III, and D. A. Smith, Acoustoelasticity: General theory, acoustic natural modes and forced response to sinusoidal excitation, including comparisons with experiment, J. Sound Vib. **52**, 519 (1977).
[48] F. Fahy and P. Gardonio, *Sound and Structural Vibration: Radiation, Transmission and Response* (Academic Press, Oxford, 1987).
[49] U. Ingard, On the theory and design of acoustic resonators, J. Acoust. Soc. Am. **25**, 1037 (1953).